Collider Physics at FNAL

John M. Butler
Fermilab
P.O. Box 500, Batavia IL 60510, USA

Abstract

After a three year hiatus, the Fermilab Tevatron Collider is back in operation delivering $p\bar{p}$ collisions at $\sqrt{s} = 1.8$ TeV. The experimental situation is considerably different this run with an upgraded CDF detector joined by the new DØ detector. Improvements to the accelerator are expected to deliver 100 pb^{-1} from a run extending into 1993. After a description of the detectors and accelerator schedule, recent physics results from the 1988-89 CDF run will be used to highlight the rich physics menu at the Tevatron.

1 Introduction

The Tevatron proton-antiproton collider at Fermilab produces the highest center-of-mass energy interactions in the world and is thus a focus for discovery level physics as well as more bread and butter topics. The collider last ran in 1988-89, where the Collider Detector at Fermilab (CDF) collected about 5 pb^{-1} of data. Currently, the Tevatron is in the midst of a run which began in May 1992 and will ultimately provide 100 pb^{-1}. This time around the experimental situation features an upgraded CDF detector and the entrance of a new, second generation collider detector DØ. This large gain in data and detection power will be applied to the collider physics menu: searching for the top quark, bottom physics, studies of QCD and jets; electroweak precision measurements; and searches for new physics beyond the Standard Model.

2 The CDF Detector

The CDF detector, shown in Fig. 1, is by now well known. A detailed description can be found in Ref. [1], so this section will focus on the upgrades to the apparatus that have been implemented for the current run. The chief components used in the analyses described later are briefly mentioned here. Surrounding the beampipe is the vertex time projection chamber (VTPC) followed by an 84 layer central tracking chamber (CTC) which measures charged particle momentum in a 1.4 T magnetic field with a precision of $\delta p_T/p_T^2 \simeq 0.001'(\mathrm{GeV/c})^{-1}$ for beam constrained tracks. Beyond the tracking chambers are electromagnetic (EM) and hadronic (HAD) calorimetry, details of angular coverage and resolutions are given in Table 1. Finally, muon chambers back up the calorimeters.

Since the 1988-89 run, CDF has made significant upgrades to the detector. They have replaced the VTPC with a new, more radiation hard version called the VTX. A central conversion detector has been added just outside the superconducting coil and will aid in distinguishing prompt photon events from the π^0 and η background. The muon system has been upgraded by adding steel and chambers in the central region to reject hadronic punchthrough and with additional chambers that extend the coverage from $|\eta| < 0.6$ to $|\eta| < 1.0$.

The upgrade that will make a large, qualitative difference is the addition of a silicon strip vertex detector (SVX)[3]. The SVX, shown in Fig. 2, consists of two 25 cm barrels which meet at $z = 0$. The detector is fairly long because

System	η range	Energy resolution
CEM	$\lvert\eta\rvert < 1.1$	$13.5\%/\sqrt{E_T} \oplus 2\%$
PEM	$1.1 < \lvert\eta\rvert < 2.4$	$28\%/\sqrt{E} \oplus 2\%$
FEM	$2.4 < \lvert\eta\rvert < 4.2$	$25\%/\sqrt{E} \oplus 2\%$
CHA	$\lvert\eta\rvert < 1.3$	$75\%/\sqrt{E_T} \oplus 3\%$
PHA	$1.3 < \lvert\eta\rvert < 2.4$	$90\%/\sqrt{E} \oplus 4\%$
FHA	$2.4 < \lvert\eta\rvert < 4.2$	$130\%/\sqrt{E} \oplus 4\%$

Table 1: Parameters of the three CDF calorimeters. CEM (CHA), PEM (PHA), and FEM (FHA) denotes the central, plug and forward EM (HAD) calorimeters [2].

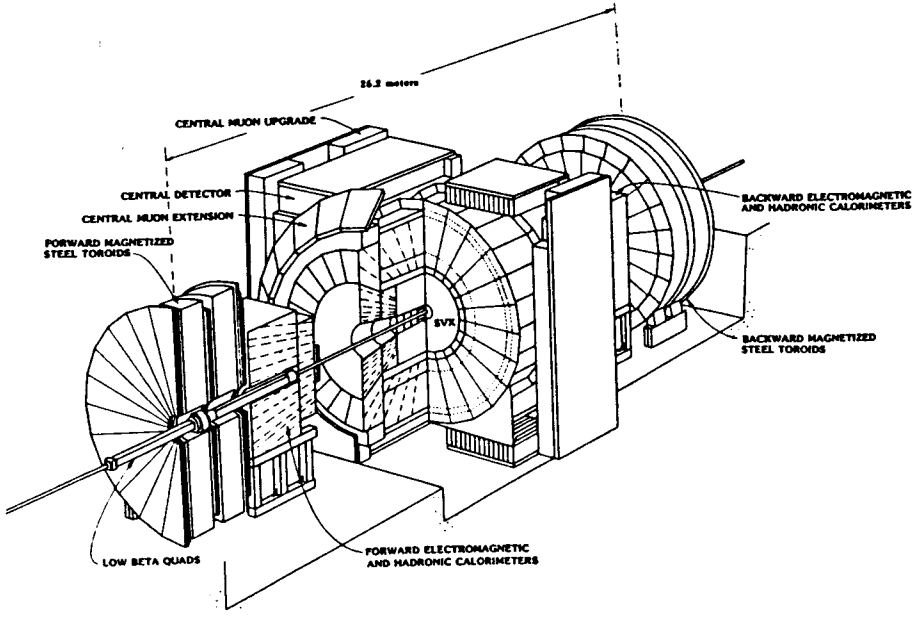

Figure 1: The CDF detector.

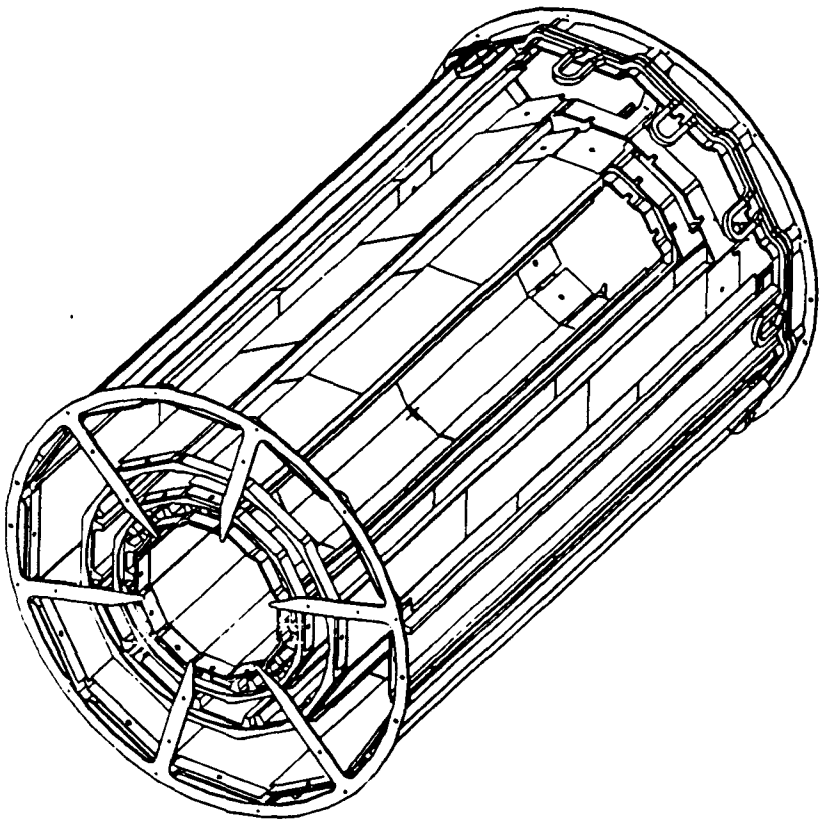

Figure 2: One half of the CDF silicon vertex detector showing four layers of silicon detectors and support structure.

the luminous region of the Tevatron has $\sigma \approx 30$ *cm* and so, even at 50 cm in length, the SVX contains only $\sim 60\%$ of the collision vertices. There are four layers of 300 μm thick silicon detectors, the three inner layers have strip pitch of 60 μm while the outer layer has 55 μm pitch. The electronics are able to integrate and store the signals from the $\sim$ 40K channels in the 3.5 μsec between beam crossings. The SVX is performing quite well, tracks are easily observed with good signal-to-noise. The results so far, without detailed alignment corrections, are already near the expected resolution for impact parameters. The SVX is an extremely promising tool for doing bottom physics in general and tagging the B's from top decay.

3 The DØ Detector

The DØ detector [4], shown in Fig. 3, is a new, second generation collider detector at the Tevatron. Since DØ has just arrived on the scene and is perhaps unfamiliar to some in the community, this section will provide a rather detailed description of the hardware. Proposed and approved in 1984, DØ has been built, commissioned with cosmic rays, rolled onto the Tevatron beamline, and is currently taking its first $\bar{p}p$ collider data. The design goal for DØ is to perform a complete survey of high p_T physics at $\sqrt{s} = 1.8$ TeV. To accomplish this goal, emphasis is placed on measuring well the fundamental objects resulting from high energy hadron collisions: leptons (electrons and muons), photons, neutrinos (as inferred by missing energy), and quarks and gluons (as they manifest themselves as jets) over the full 4π solid angle. These principles are realized by a design which consists of three major subsystems: a Central Detector package, surrounded by high quality, compact and hermetic calorimetry, and finally a full coverage muon system.

Another design choice is that there is no central magnetic field in DØ. The main advantage is that, since there is no long lever arm necessary for the trackers, the tracker can have a relatively small radius which allows the calorimetry to be more compact and hermetic. This has several benefits, for example in the measurement of jets, as well as minimizing the decay in flight of pions and kaons by interacting them as soon as possible. A disadvantage is that, without a central magnetic field, one can't use momentum analyzed charged tracks as part of the *in situ* energy calibration of the calorimeter. Also certain physics topics, such as reconstruction of B hadrons decaying

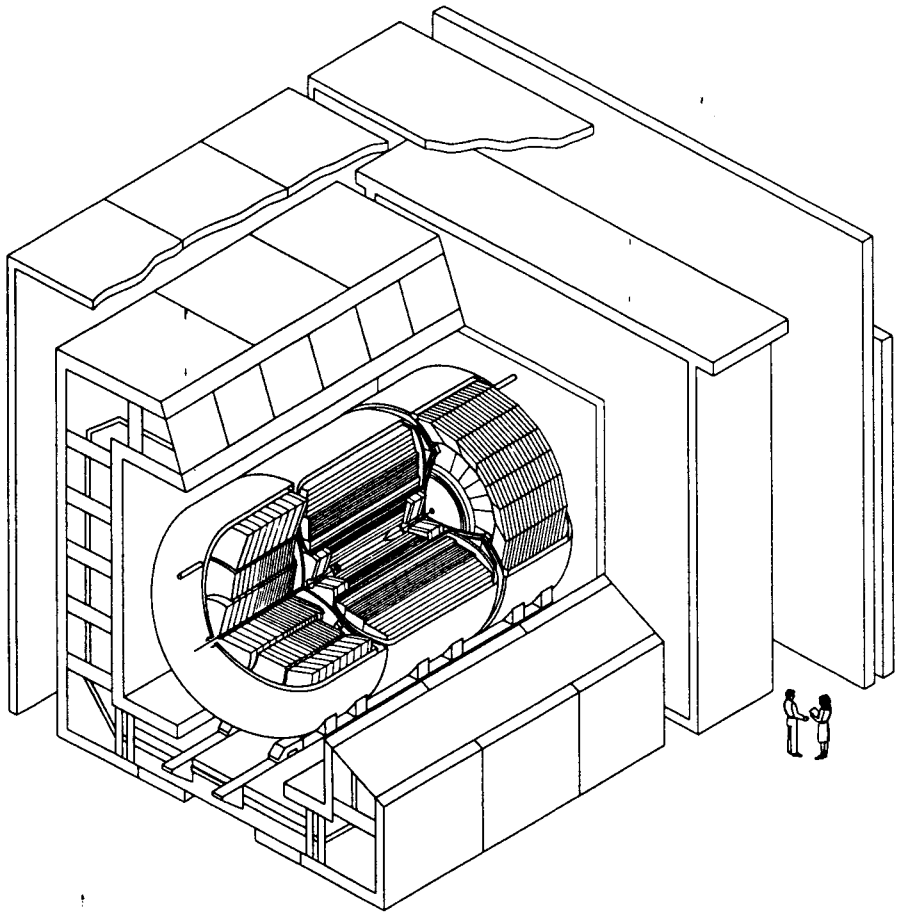

Figure 3: The DØ detector.

into multiparticle final states, are not accessible to DØ.

The major DØ subsystems will now be described.

3.1 Central Detectors

The DØ Central Detectors (CD) consist of four different wire chambers shown in Fig. 4. In the central region there are three concentric cylindrical chambers with axially strung wires. Starting from the beampipe they are the Vertex Drift Chamber (VTX) followed by a Transition Radiation Detector (TRD), and the Central Drift Chamber (CDC). In the forward and backward region there are the Forward Drift Chambers (FDC) which feature radially strung ϕ sectors and θ chambers strung along cartesian coordinates.

With no central magnetic field, the CD clearly are not used to determine charged particle momentum. Their purpose is to:

- Measure the primary vertex position and distinguish events with multiple vertices.
- Aid in the particle identification of:
  - Electrons and Photons
    1. Electron candidates require a CD track match with electromagnetic clusters in the calorimeter.
    2. Electrons (which appear as a singe minimum ionizing particle (MIP)) are separated from photon conversions ($\gamma \rightarrow e^+e^-$ (2 MIPs)) by dE/dx measurement using 100 MHz FADCs. The 2 MIP rejection is 30 : 1 with an electron efficiency of 90%.
    3. Test beam measurements show the TRD gives a pion rejection of 50 : 1 with an electron efficiency of 90%.
  - Muons: linking the CD track with the muon system track helps reject cosmics and improves the angle measurement at the primary vertex.
  - Find V^0's such as K^0's and Λ's.

Performance parameters from test beam data and early collider experience are listed in Table 2.

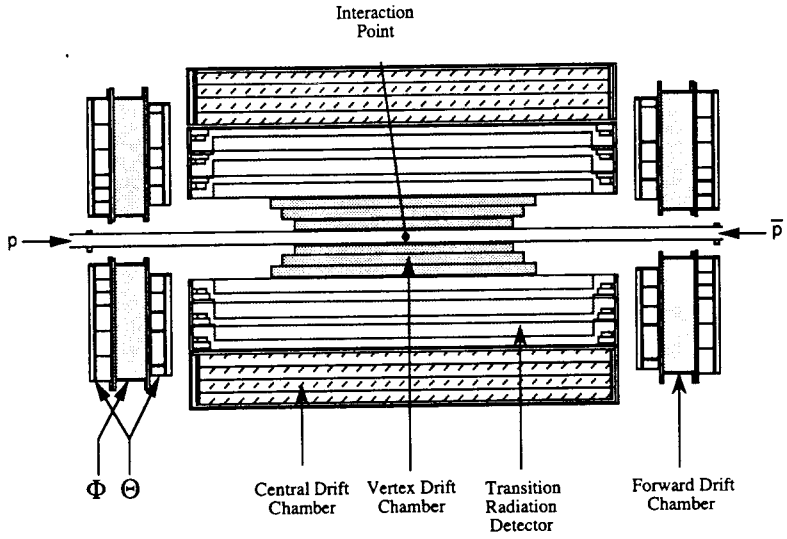

Figure 4: The DØ Central Detectors.

3.2 Uranium-Liquid Argon Calorimeters

The DØ calorimeters, shown in Fig. 5, have liquid argon as an active medium and uranium plates as an absorber. The modules are contained in three cryostats: one central calorimeter and two ends. There are three types of modules: electromagnetic, fine hadronic and a coarse hadronic tail catcher.

The calorimetry is quite hermetic, extending to $|\eta| < 4.1$ with full ϕ coverage. There is fine transverse segmentation, the tower size being $\Delta\eta \times \Delta\phi = 0.1 \times 2\pi/64 (\sim 0.1)$. To get a better position measurement for electrons and photons, the segmentation at EM shower maximum is finer still — $\Delta\eta \times \Delta\phi = 0.05 \times 0.05$. The longitudinal segmentation is also good: 8 (9) samples in depth for the central (end) calorimeter.

There has been considerable test beam work to understand the characteristics of the calorimeter modules and obtain a calibration which can then be transferred to the modules installed at DØ. Several recent results [5] will be presented from the 1990 test beam run where a set of modules was exposed to e, π, μ beams with momentum $10 - 150$ GeV.

The electromagnetic and hadronic resolutions are given by:

$$EM \ : \ \sigma/E \ = \ 15.7\%/\sqrt{E} \oplus 0.3\%$$
$$HAD \ : \ \sigma/E \ = \ 50\%/\sqrt{E} \oplus 4\% \ .$$

The calorimeter is linear to better than $\pm 0.5\%$ over this momentum range as well as being extremely stable — the response has varied by less than 0.2% in the last five months.

The choice of uranium and liquid argon allows the calorimeter to be compensating, *i.e.*, have equal response to incident electrons and pions. This is illustrated in Fig. 6 which shows that e/π ratio is approximately unity, it varies between $1.09 - 1.02$ for incident momentum $p = 10 - 150$ GeV.

Detector	VTX	CDC/FDC
$\|\eta\|$ coverage	0 - 2	0 - 1 / 1 - 3
Resolution in $r\phi$	$60\mu m$	$180\mu m$
Resolution in z	$15mm$	$2mm$

Table 2: Performance parameters for the DØ central tracking detectors.

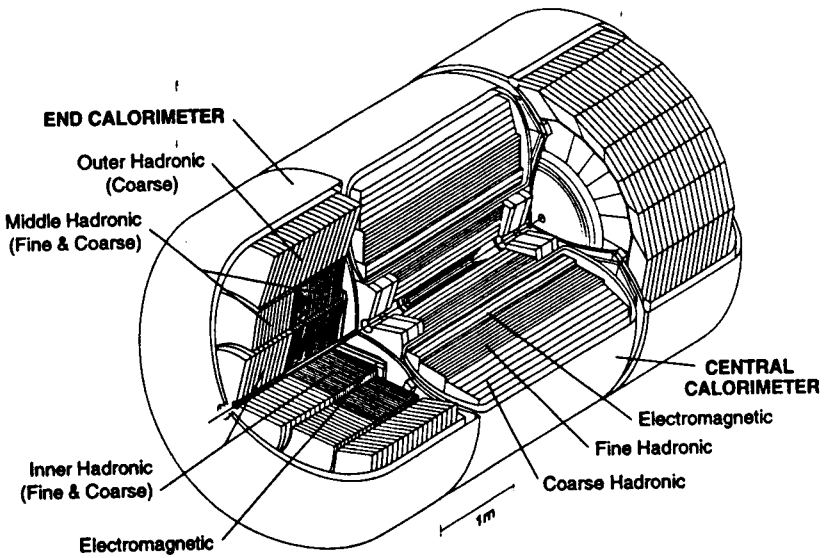

Figure 5: Isometric cutaway view of the DØ calorimeters and central detectors.

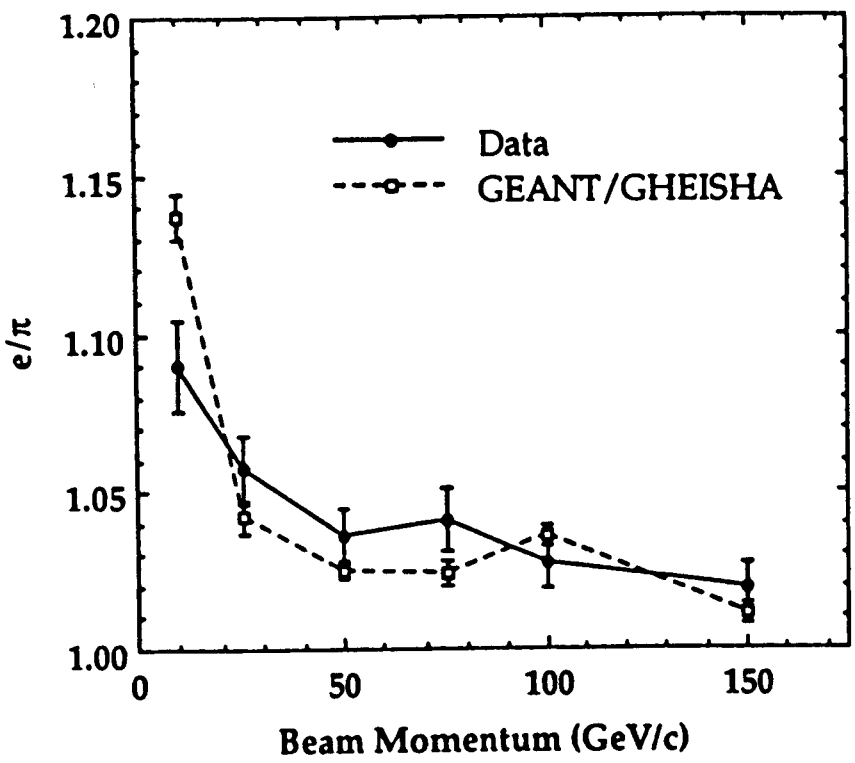

Figure 6: The ratio of electron to pion response as a function of incident momentum for the DØ calorimeter.

Two important ingredients for the identification of electrons will be discussed next. The position resolution of electromagnetic showers is measured in the third layer of the EM calorimeter where the transverse segmentation is $\Delta\eta \times \Delta\phi = 0.05 \times 0.05$. As seen in Fig. 7, the resolution scales with the expected $1/\sqrt{E}$ behavior and $\sigma < 2$ mm for electrons above 25 GeV. The good resolution permits tight track match cuts to minimize the background from random overlaps of tracks with showers from π^0's. The fine transverse and longitudinal segmentation is employed to discriminate between electron and hadron shower shapes. The pion rejection is shown in Fig. 8 where it is seen that using an H-Matrix technique gives a pion rejection of 900 – 3000 for incident momentum of 50 – 150 GeV while maintaining 95% electron efficiency.

3.3 Muon System

The DØ muon system [6] is shown in Fig. 9. The muon system consists of five magnetized iron toroids with a 1.9 Tesla field surrounded by layers of proportional drift tube (PDT) chambers. Just outside the calorimeter and inside the toroid is the A-layer, outside the toroid are the B- and C-layers separated by > 1 m to provide a lever arm for momentum determination. In the wide angle muon system, there are 4 decks of 5×10 cm tubes in the A-layer and 3 decks in the B- and C-layers allowing typically ten measurements along a track. The resolution transverse to the wire is about 0.3 mm while shaped cathode pads allow a $\sigma \approx 3$ mm determination of the position along the wire [7]. Since the particle density increases rapidly with decreasing θ, it is necessary to go to a smaller cell size at high $|\eta|$ to maintain a reasonable occupancy. This is done in the Small Angle MUon System (SAMUS) where there are 6 stations of 3 cm stainless steel tubes arranged with 3 layers/station in an xyu geometry. SAMUS has drift time readout only with a drift resolution of 0.3 mm.

The principle features of the DØ muon system are its thickness and solid angle coverage. Figure 10 shows the amount of material in interaction lengths as a function of polar angle from the beam. The A-layer sits behind typically $7 - 9$ λ while the B- and C-layers are behind about 13 λ in the central region and 19 λ in the forward region. This material protects the muon system from hadron punchthrough; the probability for punchthrough is $< 10^{-4}$ [8], which allows detection of muons near or inside jets. The solid angle coverage for

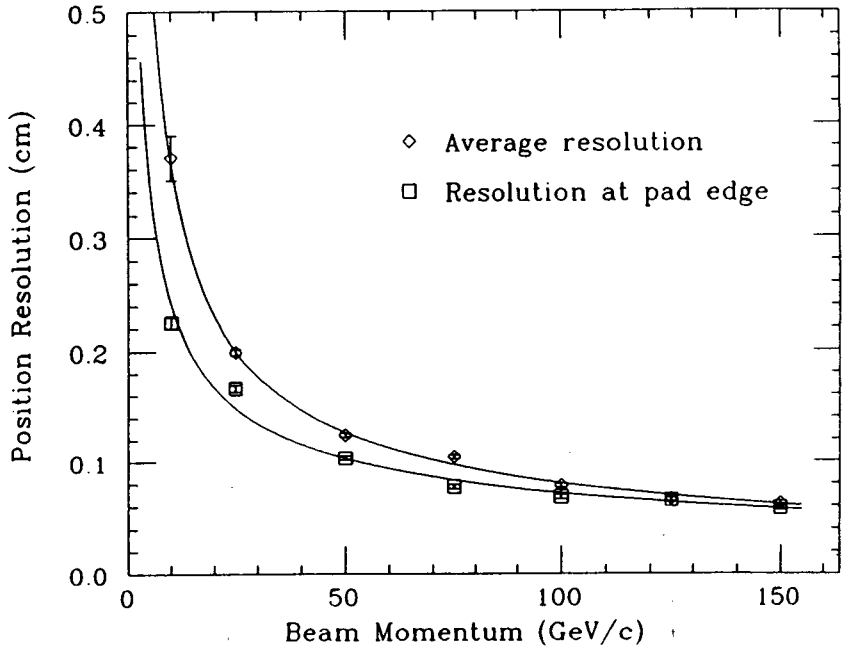

Figure 7: The position resolution of electrons in the EM calorimeter as a function of electron momentum.

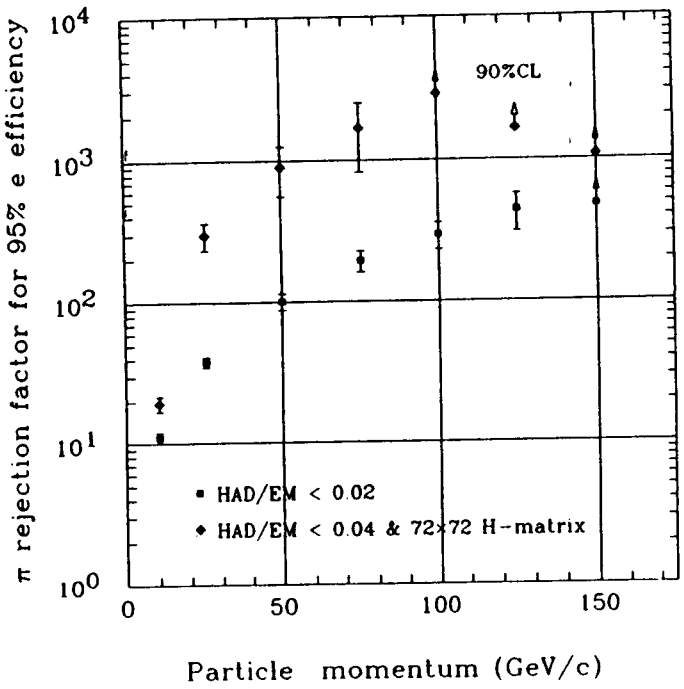

Figure 8: Pion rejection factors as a function of pion momentum. The points shown are for a simple cut on the ratio $HAD/EM < 0.02$ and for $HAD/EM < 0.04$ combined with the H-Matrix scheme.

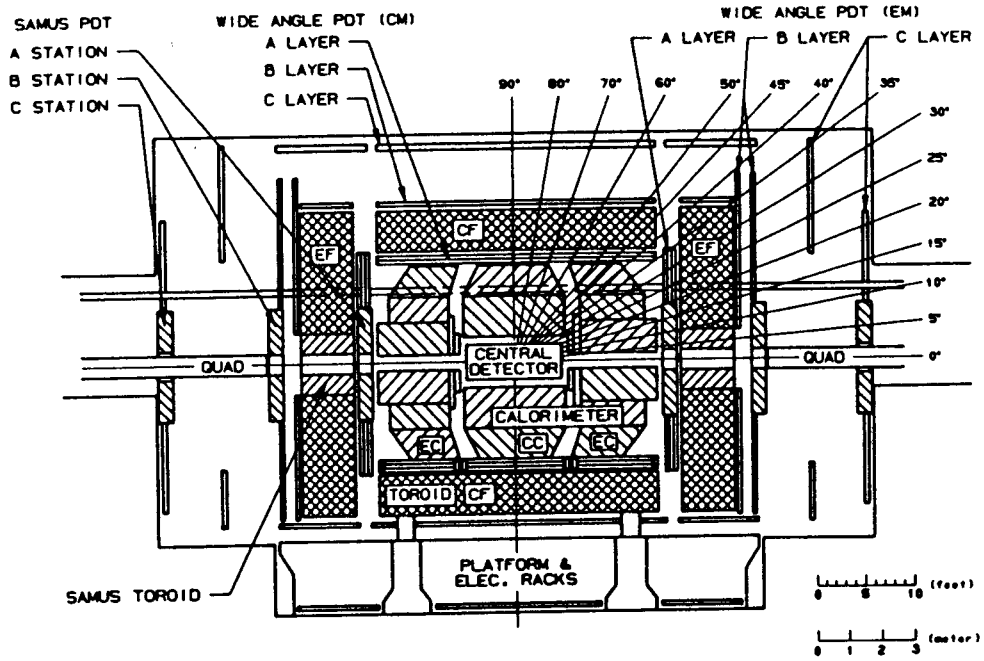

Figure 9: Elevation view of the DØ detector with the components of the muon system labeled.

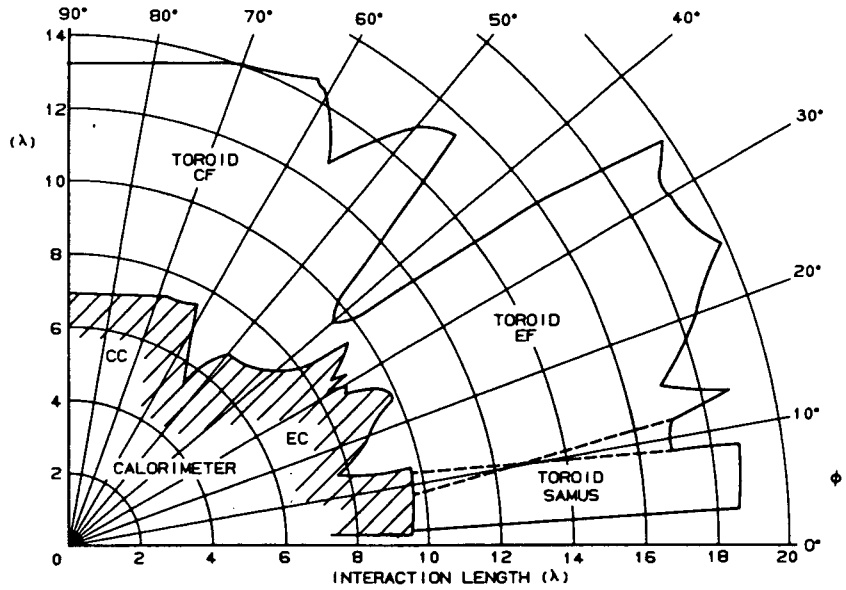

Figure 10: Total interaction length in the DØ calorimeter and muon system as a function of polar angle from the beam.

measuring a muon in all three layers extends to $|\eta| < 3.1$ which is important for certain physics topics, the prime example being b physics. To illustrate this, consider the inclusive decay $B \to \psi X$ where $\psi \to \mu^+\mu^-$. Figure 11 shows the η distribution for the ψ decay muons where it is clear that good η coverage buys a lot in statistics.

4 Tevatron Prospects

The Fermilab Tevatron is a $\bar{p}p$ superconducting collider operating with 6 on 6 proton and antiproton bunches at center-of-mass energy $\sqrt{s} = 1.8$ TeV. The last run of the Tevatron was in 1988-89 when the CDF experiment logged an integrated luminosity of approximately 5 pb^{-1}. The current run began in May 1992 and is designated Run IA. The goals for Run IA are to achieve a peak luminosity of $5 \times 10^{30} cm^{-2} s^{-1}$ and log 25 pb^{-1}. Run IA will continue until spring 1993 followed by a pause to complete the upgrade of the linac. Run IB then follows this break, there will be no intervening fixed target run, with the goals of reaching a peak luminosity of $1 \times 10^{31} cm^{-2} s^{-1}$ and logging 75 pb^{-1}. The precise splitting of the integrated luminosity is not fixed, but the aim is to have 100 pb^{-1} for the combined IA and IB runs. A summary of the runs is presented in Table 3.

Note that in Run IB the average number of interactions per crossing exceeds unity. In order to remedy this situation in going to still higher luminosity, the next step will be to increase the number of bunches in machine to 36 on 36 bunches of protons and antiprotons. A consequence of increasing the number of bunches is decreasing the interval between crossings to 400 ns or less. It is interesting to note that as the luminosity increases in the coming

Run	1988-89	IA	IB
Peak $\mathcal{L}$ $(cm^{-2}s^{-1})$	1.6×10^{30}	5×10^{30}	1×10^{31}
$\int \mathcal{L}\, dt$ (pb^{-1})	5	~ 25	~ 75
Interactions/crossing	0.3	0.9	1.5
Accelerator Improvements		Separators, $\bar{p}$ Upgrade	Linac Upgrade

Table 3: Summary of parameters of the past, current and future Tevatron runs.

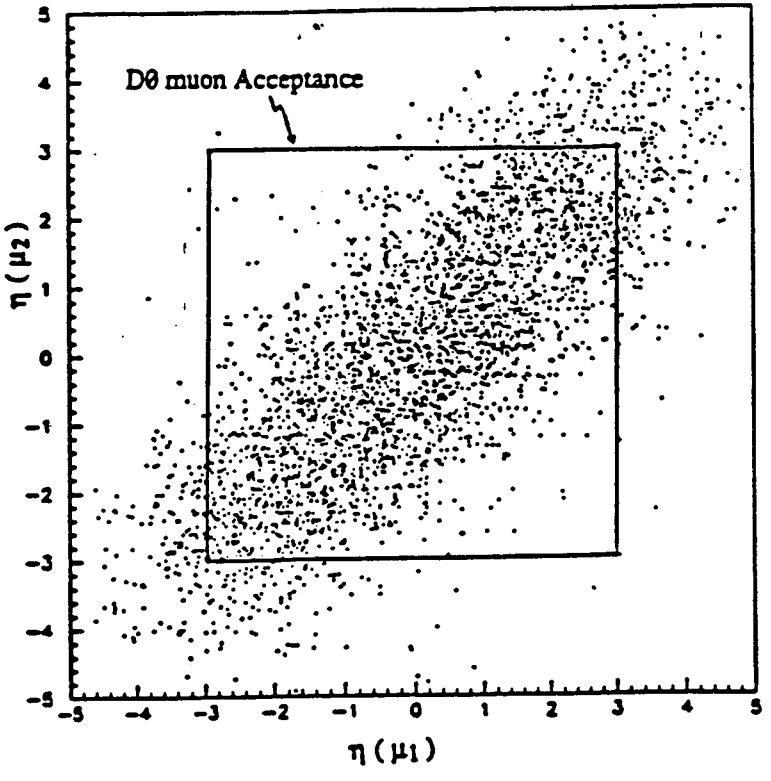

Figure 11: The η distribution of muons from the inclusive decay $B \to \psi X$ where $\psi \to \mu^+\mu^-$.

runs, CDF and DØ will be facing and finding solutions for many of the data acquisition challenges that will confront experiments at the SSC.

5 Recent Results

This section will present a selection of recent results from CDF based on data from the 1988-89 run and indicate how CDF and DØ will extend these analyses in the future. While the selection of topics will focus on high p_T physics, it should be recognized that there are many other subjects pursued by a variety of experiments at the Tevatron including the total $p\bar{p}$ cross section, single and double diffraction, and rapidity gaps to name a few.

5.1 Top Searches

The top quark is last quark in the minimal Standard Model which remains unobserved. There is, however, considerable indirect evidence for the existence of the top [9]. In fact, predicting the top mass using a cocktail of electroweak measurements has become something of a cottage industry [10]. This section will discuss the search for direct observation of the top quark.

It is assumed here that $m_t > m_W + m_b$, *i.e.*, the top decays into an on-shell W and b quark and that the branching ratio for $t \to Wb$ is 100%. Once $m_t > m_W + m_b$, the dominant production mechanism for top in $p\bar{p}$ collisions is $t\bar{t}$ pair production. A recent calculation of the $t\bar{t}$ cross section as a function of m_t is shown in Fig. 12 for Tevatron energies [11]. To illustrate the experimental difficulties involved as m_t becomes large, let's assume a "reasonable" top mass of $m_t = 140$ GeV. From Fig. 12, $\sigma(p\bar{p} \to t\bar{t}X) \approx 15\ pb$ which implies only about 1500 events *produced* in all of Runs IA and IB with $\int \mathcal{L}dt = 100\ pb^{-1}$. Folding in the branching ratio from Table 4 to a promising final state like $e\mu$ and a typical detection and reconstruction efficiency of $\epsilon \sim 15\%$, only 6 events remain. Clearly, top physics at the Tevatron will always be constrained by limited statistics.

The limited statistics color the search strategies for top. Given the small number of events in a given decay mode, the unambiguous discovery of top will likely involve the combination of several modes with the yields all consistent with originating from top. Making the job more difficult is the fact that the decay modes with the least background also have the lowest branch-

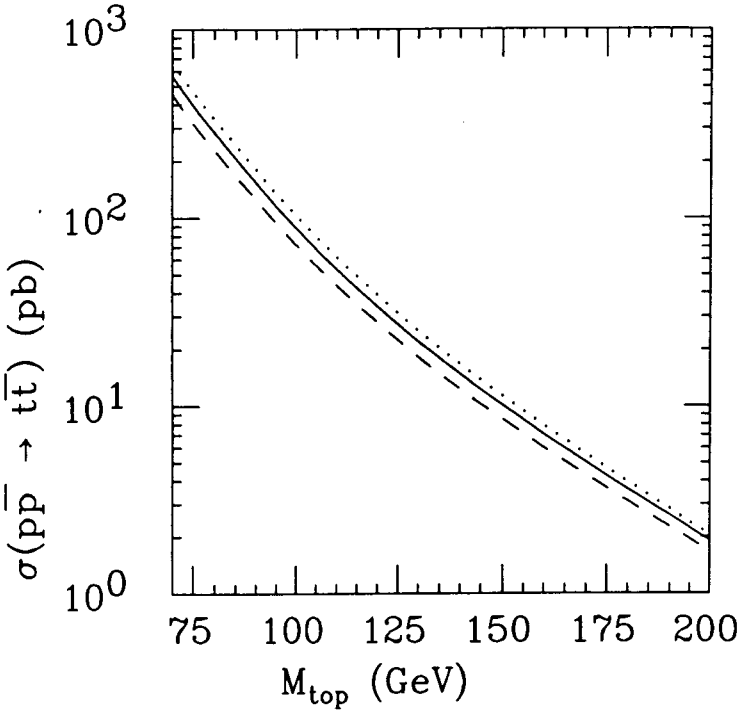

Figure 12: Top cross section vs. m_t at $\sqrt{s} = 1.8$ TeV (from Ref. [11]).

$W_1 \rightarrow$ $W_2 \downarrow$	$e\nu$	$\mu\nu$	$\tau\nu$	jets
$e\nu$	1/81	1/81	1/81	6/81
$\mu\nu$	1/81	1/81	1/81	6/81
$\tau\nu$	1/81	1/81	1/81	6/81
jets	6/81	6/81	6/81	36/81

Table 4: Branching ratios for $t\bar{t} \rightarrow W_1 W_2 b\bar{b}$.

ing ratios. The channels fall into three categories labeled by the W decay products; in order of increasing difficulty they are:

- *Dileptons:* $e\mu$ being the best, followed by ee and $\mu\mu$. Although $W \rightarrow \tau\nu$ has been seen by CDF [12], top decay modes with τ's have not been considered to date.
- *Lepton + Jets:* where the lepton is e or μ. Here the non-trivial $W + jets$ background must be dealt with.
- *All Jets:* the overwhelming QCD background will require sophisticated analysis techniques to dig out a signal, the 44% branching ratio provides the incentive. This mode is for those who find the others too easy.

CDF has recently published an extensive account of their search for top with an integrated luminosity of 4.1 pb^{-1}. The following will attempt to give a flavor of the analysis, for details see Ref. [2].

5.1.1 $t\bar{t} \rightarrow$ *Dileptons*

The $e\mu$ channel has the lowest background and is likely to be the first channel where an unambiguous signal for top is seen. The principal backgrounds and cuts used to eliminate them are:

- QCD production of heavy flavors $b\bar{b}$ and $c\bar{c}$ which decay semileptonically. Requiring the e and μ be isolated and have $p_T^\mu, E_T^e > 15$ GeV effectively removes the tail of this low p_T background.

- The decay $Z \rightarrow \tau\tau$ where the τ's subsequently decay to $e\mu$. Because the τ mass is small compared to M_Z, the majority of the $e\mu$ pairs will be back-to-back in the transverse plane and a cut of $\Delta\phi_{e\mu} < 160°$ removes these events.

- Diboson WW, WZ production; here one is saved by the low cross section, of order 10 pb, however this background will become troublesome for top masses of 150 GeV or more.

CDF has observed one candidate event in 4.1 pb^{-1}, with a background estimate of 1.2 ± 0.5 events. The backgrounds mentioned above contribute fractions of an event while the largest source is from a QCD jet or $W + jets$ event with a misidentified lepton. With one event observed in the signal region, an upper limit can be placed on the top production cross section which can then be translated into a lower limit on the top mass using a calculation *à la* Fig. 12, this works out to be $M_t > 72$ GeV at 95 % confidence level.

The ee and $\mu\mu$ channels have the same backgrounds as $e\mu$ and the same cuts are applied. In addition, there are the following backgrounds to deal with:

- Drell-Yan production of dileptons. Since the production is predominately low p_T, the leptons are back-to-back in the transverse plane and the $\Delta\phi_{e\mu} < 160°$ cut is also effective here. Top events will have two stiff neutrinos while Drell-Yan has no missing energy so a $\not\!\!E_T > 20$ GeV cut removes the residual background from this source.

- $Z \rightarrow \ell^+\ell^-$ is removed by a simple cut on the dilepton mass of $75 < M_{ll} < 105$ GeV.

CDF observed no candidates passing these cuts, the background estimate is 1.5 ± 0.8 events. Combining the $e\mu, ee, \mu\mu$ channels together, a limit from dileptons of $M_t > 85$ GeV at 95 % confidence level is obtained.

5.1.2 *Lepton + Jets*

The event selection for this channel is to require the lepton (e or μ) to have $E_T^e, p_T^\mu > 20$ GeV, missing energy $\not\!\!E_T > 20$ GeV and ≥ 2 jets with $E_T > 10$ GeV. These criteria are efficient for top but unfortunately also for W's produced with jets. The transverse mass shape for the 104 $e + jets$ and 91 $\mu + jets$ events selected agrees well with the $W + 2$ *jet* Monte Carlo. To discriminate the relatively small top signal from the $W + jets$ background, another handle is necessary. CDF looks for additional muons in the event from the decays of b or c quarks from top. There are 8 events from the above sample with a muon satisfying a $2 < p_T < 15$ GeV cut. A final cut requiring the muon be separated from the two highest E_T jets (presumably the hadronic decay products of the other W) reduces the fake μ contamination from punchthrough. No candidates survive all cuts where 1.6 (1.1) events are expected from $p\bar{p} \rightarrow t\bar{t}$ for $M_t = 90(100)$ GeV.

Combining the results from $e\mu, ee, \mu\mu$ and *Lepton + Jets + b Tag* gives the final CDF limit from 4.1 pb^{-1} of $M_t > 91$ GeV at 95 % confidence level. Figure 13 shows the results of all these analyses.

5.1.3 What's Next?

For Run IA, a factor of about five in integrated luminosity and two detectors in the hunt will allow sensitivity to top masses up to 120 - 130 GeV. For CDF, the new muon chambers have 40% more acceptance for $e\mu$. The SVX will be used to tag $b \rightarrow jet$ in the $\ell + jets$ with efficiency similar to the soft muon tag described above. DØ brings a full acceptance for electrons and muons from top, and the fine calorimeter segmentation is good for sorting out the numerous jets in top events.

A reasonable rule-of-thumb guide for top search reach is given in Fig. 14 [13]. It shows the integrated luminosity needed to find top in the $e\mu$ and *Lepton + Jets* channels as a function of top mass. Combining that with the Standard Model prediction of $M_T \lesssim 220$ GeV and the expected integrated luminosity provided by the Tevatron in the 1990's, CDF and DØ will either find the top quark or find indications of new physics by the end of the decade. Either possibility is exciting!

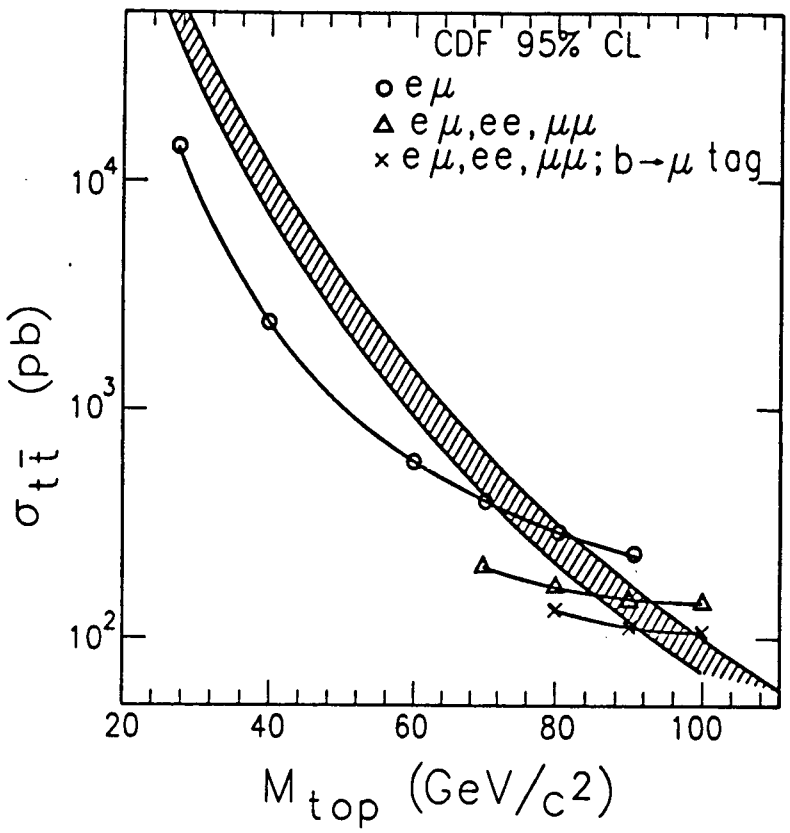

Figure 13: The upper limits on $t\bar{t}$ cross section from the CDF $e\mu, ee, \mu\mu$ and *Lepton + Jets + b Tag* analyses are shown. The shaded band represents the range of theoretical predictions. The 95% CL limit comes from the intersection of the $\sigma_{t\bar{t}}$ limit with the lower bound from theory.

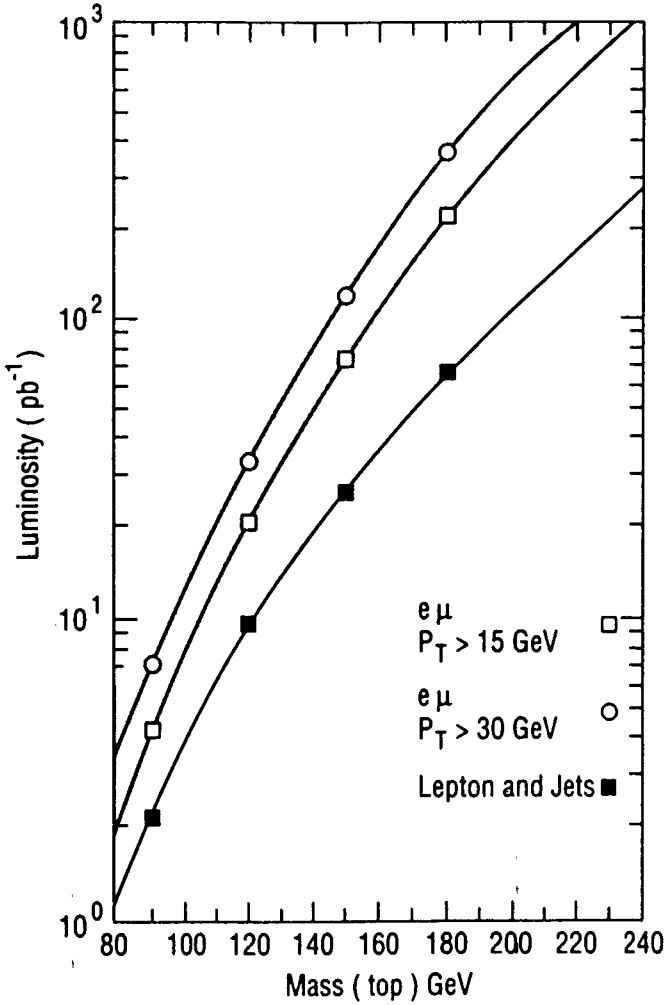

Figure 14: Required luminosity to discover top at $\sqrt{s}$ = 1.8 TeV for two decay modes.

5.2 Bottom Physics

Given the fine work done at the e^+e^- storage rings, it is worthwhile to motivate doing bottom physics at the Tevatron. The overriding reason is that a tremendous number of $b\bar{b}$ pairs are produced at hadron colliders. For example, for $\int \mathcal{L}\, dt = 100\ pb^{-1}$ and a cross section of $\sigma(b\bar{b}) \approx 40\ \mu$b at Tevatron energies, $4 \times 10^9\ b\bar{b}$ pairs are produced. Clearly, until the advent of next generation B Factories, bottom physics topics which require very high statistics are a natural for the Tevatron. The experimental challenge of digging the b's out of the data is, however, nontrivial. The results from CDF, some of which are described below, indicate that very clean B meson signals can be obtained. This has opened the door to a new era for the collider program where b physics has become the focus for upgrades to CDF and DØ through the end of the decade.

In order to extract a clean sample of bottom decays from the large light quark background, two trigger strategies have been devised:

- Tag $b \to \ell\nu X$ decays by requiring a moderate p_T lepton.
- Tag $B \to \psi X$ using an inclusive ψ sample. It is necessary to unfold the ψ's from B hadrons from direct charmonium. This is accomplished by recognizing that ψ's from $\chi \to \psi\gamma$ are produced with low p_T while ψ's from B's have characteristic p_T of order m_b. As shown in Ref. [14], ψ's from B's dominate for p_T above about 7 GeV.

5.2.1 b Cross Section

The measurement of the b cross section is interesting for a number of reasons:

- As a test of QCD calculations by determining $\sigma(b\bar{b})$ as a function of kinematic variables such as x and p_T. This would help distinguish the contribution of the various production mechanisms: lowest order $2 \to 2$ processes versus higher order but numerically large gluon splitting.
- It is crucial to understand $\sigma(b\bar{b})$ as a function of p_T in that it constitutes a background for top.
- It provides an "engineering number" for planning Tevatron detector upgrades designed to do bottom physics and understanding rates at future hadron colliders such as the SSC and LHC.

CDF has used a combination of inclusive and exclusive measurements to determine $\sigma(b)$ as a function of p_T of the b: the inclusive electron p_T spectrum, the semi-leptonic decay $B^\pm \to e^\pm \nu D^0 X$, inclusive ψ and ψ' measurements, and the decay $B^\pm \to \psi K^\pm$. The latter analysis [15] will be discussed briefly here.

The analysis employs the second trigger strategy discussed above, namely tagging B's with high p_T ψ's. From an integrated luminosity of $2.6\ pb^{-1}$, CDF selects events with two oppositely charged muon candidates with $p_T > 3$ GeV each. The resulting dimuon mass plot is shown in Fig. 15 and yields a very clean signal of 1029 ± 37 reconstructed ψ's over a background of only 128 $\mu^+\mu^-$ pairs. In the absence of kaon identification, CDF defines candidate kaons as any charged track with $p_T > 2.0$ GeV. The resulting $\mu^+\mu^- K^\pm$ mass distribution is shown in Fig. 16 with a peak of 14.1 ± 4.3 events in the $B^\pm$ mass region, the first fully reconstructed B's from a hadron collider.

Using this signal and the branching ratios for $B(B^- \to \psi K^-)B(\psi \to \mu^+\mu^-)$ from CLEO and ARGUS, a cross section for $B^- \to \psi K^-$ can be extracted: $\sigma(p\bar{p} \to B^- X; p_T > 9\ GeV, |y| < 1.0) = 2.8 \pm 0.9 \pm 1.1\ \mu b$. Rather less straightforward is to unfold this cross section to obtain the b quark cross section. It is necessary to assume the relative fragmentation of the b quark into the various bottom hadrons, CDF uses a fairly standard assumption that the ratio $B^- : \bar{B}^0_d : \bar{B}^0_s : b$ baryons is given by 0.375:0.375:0.15:0.10. As will be mentioned later, measuring this ratio is a goal for the present and future collider runs. The other necessary ingredient is relating the B^- p_T to that of the b quark. The method chosen is to quote a cross section for b quarks with $p_T > p_T^{min}$ where p_T^{min} is defined as the b quark p_T for which 90% of the reconstructed B^-'s in the final sample originate from b quarks with $p_T > p_T^{min}$. Following this prescription for B^-'s with $p_T > 9$ GeV, one finds $p_T^{min} = 11.5$ GeV. The result of this unfolding is the cross section $\sigma(p\bar{p} \to bX; p_T > 11.5\ GeV, |y| < 1.0) = 6.1 \pm 1.9 \pm 2.4\ \mu b$.

5.2.2 Search for Λ_b

The Λ_b is a baryon made up of bdu quarks and its discovery has a rather checkered past. First observation was claimed in 1981 and subsequently disputed [16], the Λ_b has emerged again in a recent analysis by the UA1 collaboration [17]. UA1 has looked for the decay mode $\Lambda_b \to \psi\Lambda$ where $\psi \to \mu^+\mu^-$ and $\Lambda \to p\pi^-$. In $4.7\ pb^{-1}$ they find 1370 ± 39 events containing

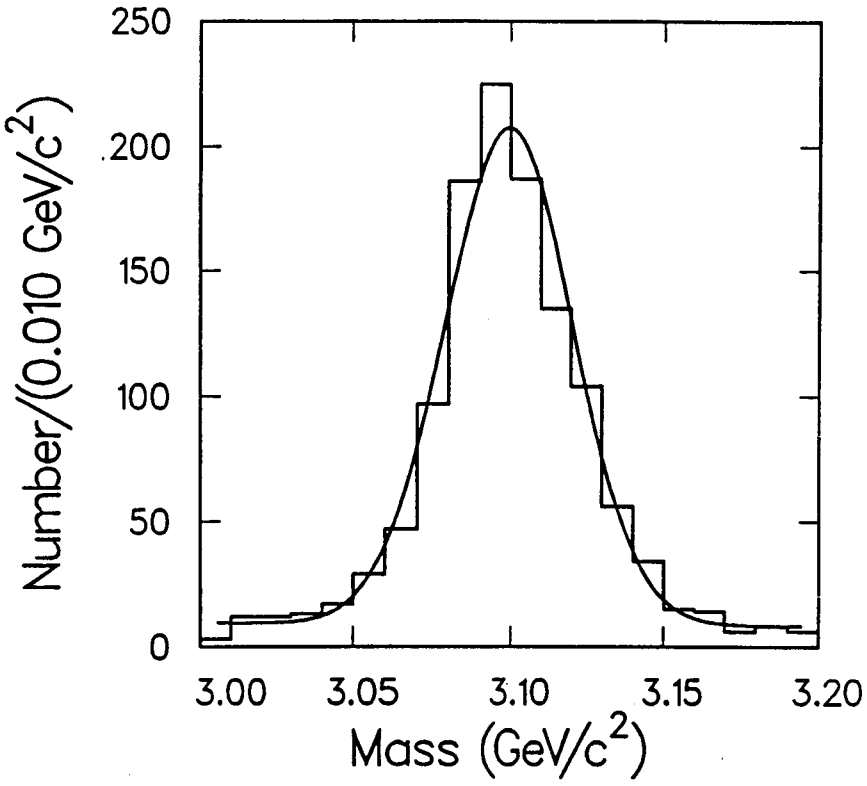

Figure 15: CDF $\mu^+\mu^-$ mass distribution showing a clean ψ signal with very little background.

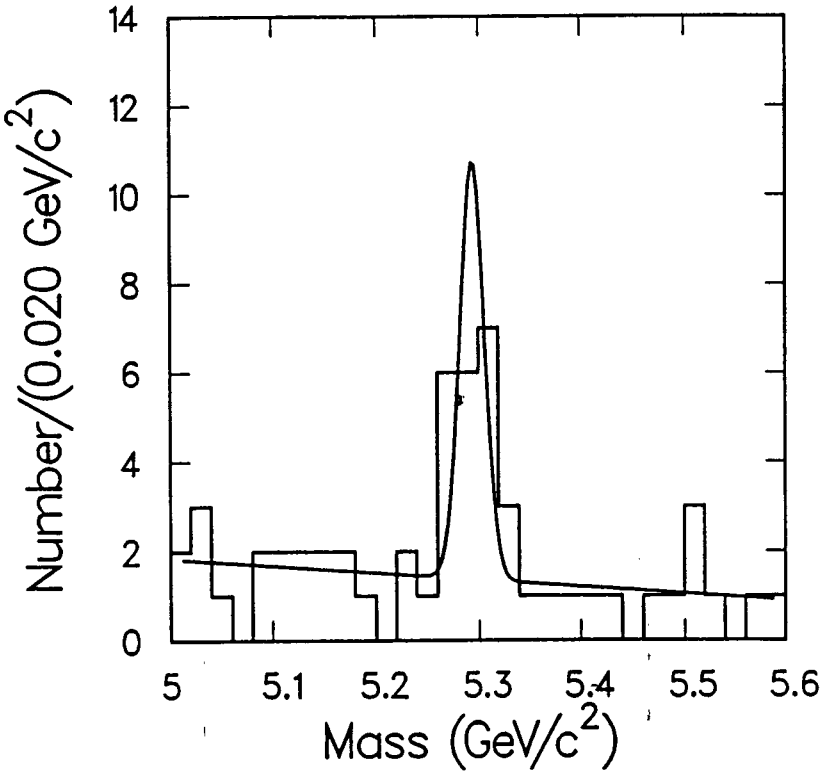

Figure 16: CDF $\mu^+\mu^- K^\pm$ mass distribution showing a signal from $B^\pm \rightarrow \psi K^\pm$.

$\psi \to \mu^+\mu^-$ with $p_T > 5$ GeV in the rapidity range $|y| < 2$. Of these events, 69 ± 11 events also have a $\Lambda \to p\pi$ decay where the Λ is required to have $p_T > 0.5$ GeV. In addition there is a cut to remove Λ's from the opposite jet by requiring $\Delta R^2 < 5$ between the Λ and ψ, where $\Delta R^2 = \Delta\phi^2 + \Delta\eta^2$. After these selection criteria are applied, there is a narrow peak of 16 ± 5 events in the $\psi\Lambda$ mass plot over a background of 9 ± 1 events, yielding a 5σ effect. UA1 measures a mass of $m_{\Lambda_b} = 5640 \pm 50 \pm 30$ MeV and a production fraction times branching ratio of $f_{\Lambda_b} B(\Lambda_b \to \psi\Lambda) = (1.8 \pm 1.1) \times 10^{-3}$.

CDF has made a similar analysis to search for $\Lambda_b \to \psi\Lambda$ in a 4.4 pb^{-1} sample [18]. As discussed previously, they ran a dimuon trigger requiring each muon to have $p_T > 3$ GeV which produced a ψ signal of 2990 ± 80 events. In this sample, 256 ± 30 events with $\Lambda \to p\pi^-$ are seen, more than four times the UA1 sample, but the $m_{\psi\Lambda}$ mass plot shows no evidence for a Λ_b peak. This nonobservation translates into a limit on production fraction times branching ratio of $f_{\Lambda_b} B(\Lambda_b \to \psi\Lambda) < 0.81 \times 10^{-3}$ (95% CL). CDF offers a possible explanation for the discrepancy, that the true CDF acceptance for Λ_b is smaller than presently calculated because the actual p_T spectrum of Λ_b is softer than found in the Monte Carlo models. The effect is that the Λ from Λ_b is so soft that the decay products curl up in the CDF tracker and are not identified, resulting in a lower acceptance than expected. With the large data sample being collected in Run IA, it will be interesting to see if the Λ_b remains elusive.

5.2.3 What's Next?

The following are some of the bottom physics topics CDF and DØ hope to address with $\int \mathcal{L}\, dt = 100\ pb^{-1}$:

- *Production Mechanisms*: taking advantage of large geometric acceptance and ability to trigger on single muons at low p_T, DØ will measure the b cross section and production dynamics.
- *Exclusive Final States*: starting from their inclusive ψ sample, CDF will search for a number of exclusive final states. In $B_s \to \psi\phi$ where $\phi \to K^+K^-$, a few hundred reconstructed decays are expected. This would be the first observation of the B_s and allow a measurement of its mass. Another channel would be to continue the search for $\Lambda_b \to \psi\Lambda$.
- $B^0, B^\pm$ *Lifetimes*: CDF expects to reconstruct about 2500 charged and neutral B decays in the SVX using currently observed modes.
- *Rare Decays*: the large production rate of b's enables the search for rare decays by means of a fairly low rate multilepton trigger. Examples are:
  - $B_c^+ \to \psi\mu^+\nu \to \mu^+\mu^-\mu^+\nu$, although the fraction of b's hadronizing as B_c's is small, this decay is Cabbibo allowed so the branching ratio to $\psi\mu^+\nu$ should be sizeable.
  - $B_d^0 \to \mu^+\mu^-$, the branching ratio is estimated to be of order 10^{-8}, limits will be pushed into the $10^{-6} - 10^{-7}$ regime.
  - Electroweak "Penguins" such as $B_d^0 \to K^{*0}\mu^+\mu^-$.

5.3 QCD

The goal of QCD studies in collider physics is to extend beyond the current situation where there is good qualitative agreement between experimental results and theory to the point where experiment challenges theory quantitatively. Recent progress in this direction has been achieved due to a large set of data from the last Tevatron run and from the advent of next-to-leading-order ($O(\alpha_s^3)$) QCD calculations [19]. The results of the NLO calculations are less sensitive to the choice of scale than leading order calculations and therefore have a smaller systematic uncertainty.

5.3.1 Inclusive Jet Cross Section

CDF has measured the inclusive jet cross section $\sigma(p\bar{p} \to jet + X)$ [20] over seven orders of magnitude, from 35 to 450 GeV in E_T. Jets are identified using a cone algorithm with a radius $R = \sqrt{\Delta\eta^2 + \Delta\phi^2} = 0.7$ in the rapidity range $0.1 \leq |\eta| \leq 0.7$. The jet E_T is then corrected for calorimeter energy response, underlying event energy in the cone, and energy resolution smearing. The resulting jet E_T spectrum is shown in Fig. 17 with the NLO QCD prediction. Figure 17 also shows the comparison to theory for a number of parton distribution functions, where the data is sufficiently precise to essentially rule out the HMRS-E set.

The jet E_T spectrum can be used to put limits on quark substructure, usually parameterized as a contact term with characteristic strength Λ_c. The

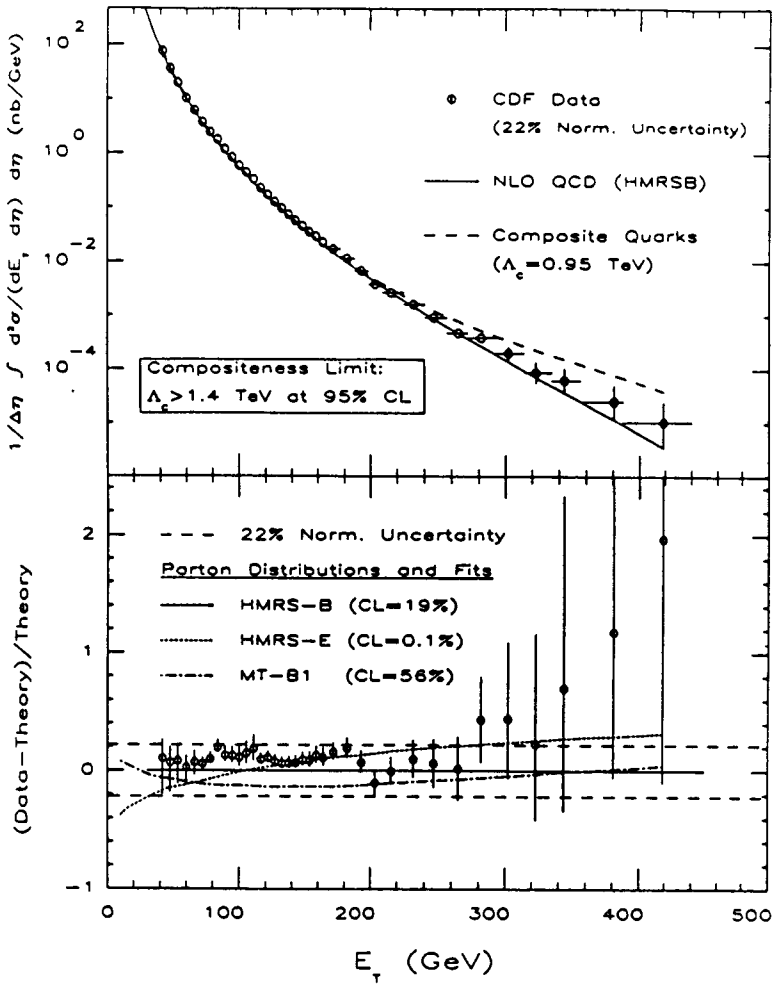

Figure 17: Upper figure: Inclusive jet E_T spectrum for cone size of $R = 0.7$ in the rapidity range $0.1 \leq |\eta| \leq 0.7$. The curve is a NLO QCD prediction using the HMRS-B parton distribution functions. Lower figure: A comparison to theory as a ratio (Data - Theory)/Theory where the HMRS-B parton distribution functions are used as a reference. Several sets of parton distribution functions are fit to the data with the results indicated.

contribution of the contact term to the spectrum is E_T independent so the effect would be to see a flattening of the spectrum at high E_T. CDF finds a limit on the compositeness scale of $\Lambda_c > 1.4$ TeV at 95% confidence level, improving on the previous limit of $\Lambda_c > 825$ GeV from UA2 [21].

With new data, CDF and DØ will continue these studies out to higher jet E_T. One of the DØ goals is to investigate the rapidity dependence of the inclusive jet cross section, for $|\eta| \gtrsim 1$ the UA2 data has shown significant discrepancies with the QCD predictions [21].

5.3.2 Prompt Photon Cross Section

Prompt photons provide a good probe of hard interactions since there is not the complication one has with jets of unfolding the hadronization. In particular, the prompt photon cross section is a sensitive measure of the gluon structure function.

CDF has measured the prompt photon cross section as a function of photon p_T [22]. To cover a large p_T range, data was collected with a prescaled low threshold trigger, $p_T > 10$ GeV ($0.1\ pb^{-1}$), and a high threshold trigger, $p_T > 23$ GeV ($3.3\ pb^{-1}$). The photon candidates are required to have $HAD/EM < 0.125$, and be isolated – extra E_T in a cone of $R = 0.7$ less than 2 GeV. Additional cleanup to reject π^0 and η background is performed using transverse shower shape and looking for photon conversions in the outer wall of the central tracker using drift tubes just outside the tracker. After all cuts, the sample is still about 50% π^0, η so a careful background subtraction is made in each p_T bin to produce the final result shown in Fig. 18. The curve in Fig. 18 is a NLO QCD prediction using the KMRS-B_0 parton distribution functions. Also shown is the UA2 result at $\sqrt{s} = 630$ GeV where it is interesting to note the data has a steeper slope at low p_T, than the QCD prediction in both data sets. This disagreement could be due to the parton distribution functions and/or problems with the calculation in dealing with bremsstrahlung at low p_T.

For the current run, the addition of a central conversion detector will greatly enhance the CDF prompt photon detection capability. As in the case of inclusive jets, DØ will rely on the good segmentation and angular coverage of its calorimeter to push the prompt photons analysis to high $|\eta|$ and low p_T to maximize the sensitivity to the gluon distribution function [23].

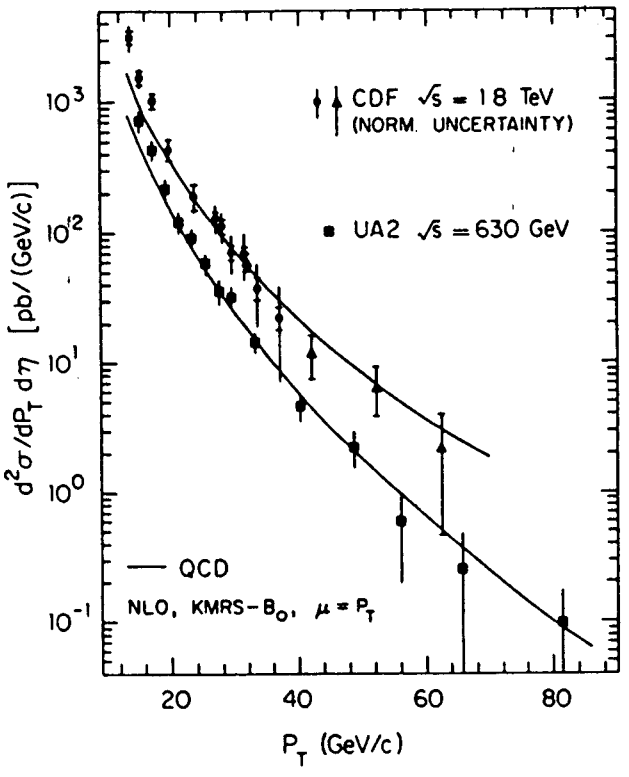

Figure 18: The isolated prompt photon cross section from CDF and UA2. The curves are NLO QCD predictions.

5.3.3 Photon-Jet Angular Distribution

In addition to the cross section, CDF has considered events with a prompt photon and a jet and measured the photon–jet angular distribution [24]. This analysis used the high threshold trigger, $p_T > 23$ GeV, and required tight isolation on the photon. At high p_T the dominant production of prompt photon events is via t–channel exchange of a spin 1/2 quark, which results in a ~flat distribution in $\cos\theta^*$, while jet–jet proceeds through t–channel exchange of a spin 1 gluon, which gives a distribution like Rutherford scattering. This picture is verified by the data as shown in Fig. 19, where the jet–jet data peaks at large $\cos\theta^*$ and the prompt photon data show only mild $\cos\theta^*$ dependence. The disagreement of the prompt photon distribution at large $\cos\theta^*$ has the same source as the disagreement seen in the cross section measurement at low p_T.

5.4 Electroweak

CDF has previously measured the cross section times branching ratios for W and Z to electrons [25]; recently they have added the muon decay modes [26]. The measurement of these cross sections is interesting because it tests Standard Model couplings, the contributions from higher order QCD and structure functions. Also the W width $\Gamma(W)$ can be extracted from the cross section ratio:

$$\underbrace{\frac{\sigma_W \cdot B(W \to \ell\nu)}{\sigma_Z \cdot B(Z \to \ell\ell)}}_{Measure} = \underbrace{\frac{\sigma(p\bar{p} \to WX)}{\sigma(p\bar{p} \to ZX)}}_{Theory} \frac{\Gamma(W \to \ell\nu)}{\Gamma(W)} \underbrace{\frac{\Gamma(Z)}{\Gamma(Z \to \ell\ell)}}_{LEP} .$$

The W width can be used to constrain unobserved W decays; in particular the decay $W^+ \to t\bar{b}$ where top then decays to a charged Higgs would have evaded direct top searches to date. The results for muons, electrons and combined are given in Table 5. Figure 20 shows the $\Gamma(W)$ dependence on top mass and the CDF results which provide a decay-mode-independent limit of $M_{top} > 45$ GeV at 95% confidence level.

Electroweak physics is a field of precision measurements and Tevatron results so far have been statistics limited. For example, the systematics for W's are often estimated using Z's. Since one has about an order of magnitude less Z's than W's, the W systematic error is usually limited by

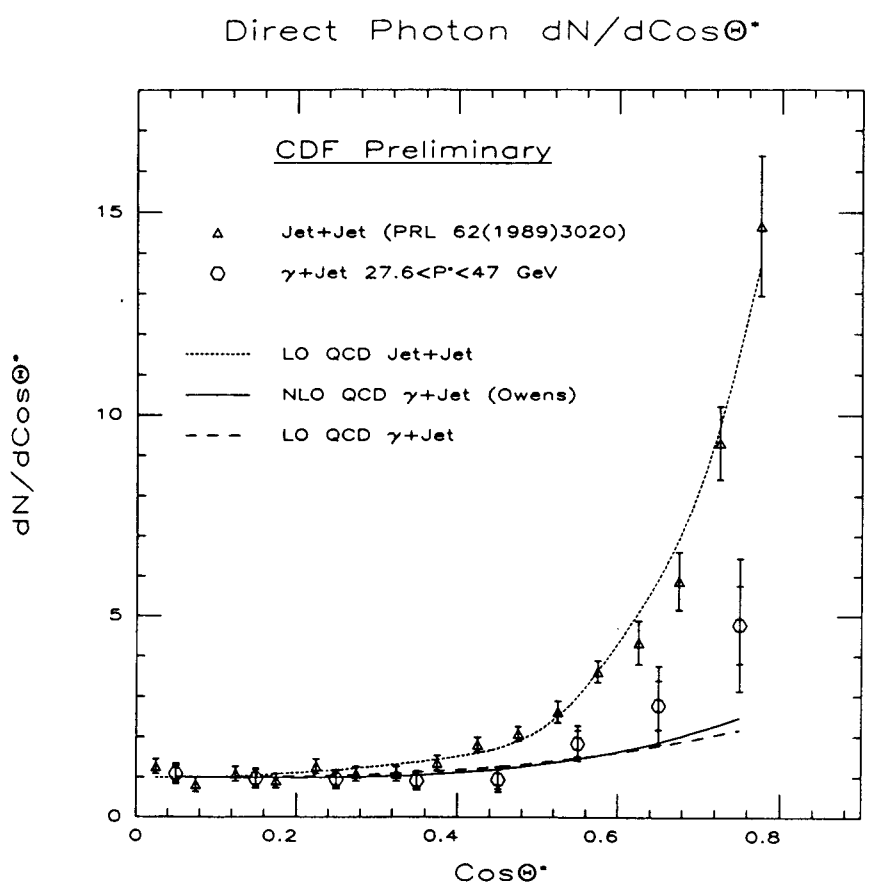

Figure 19: CDF photon–jet angular distribution compared with the jet–jet angular distribution and leading order and NLO QCD calculations.

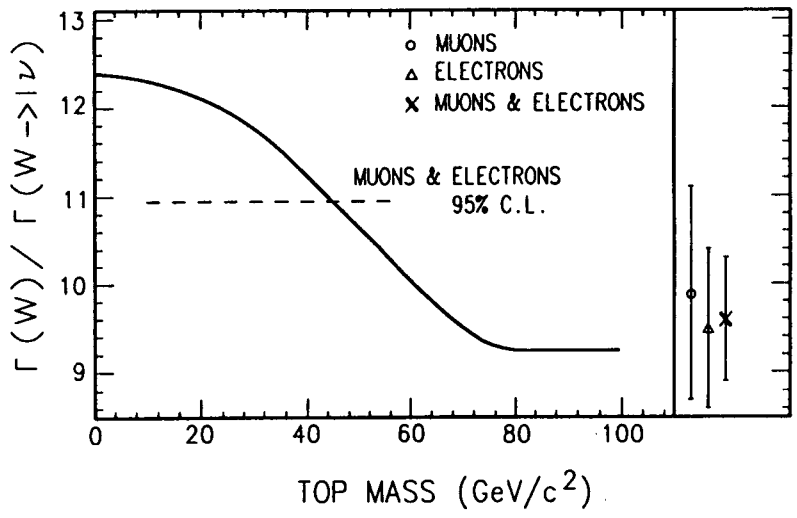

Figure 20: Theoretical prediction for the inverse W branching ratio to leptons as a function of top mass. The CDF results for muon, electron, and combined measurements are indicated along with the top mass limit derived from the combined result.

	Muons	Electrons	Combined
	Statistical, systematic, and luminosity errors.		
$\sigma(W) \cdot B$ (nb)	$2.21 \pm 0.07 \pm 0.14 \pm 0.15$	$2.19 \pm 0.04 \pm 0.14 \pm 0.15$	$2.20 \pm 0.04 \pm 0.13 \pm 0.15$
$\sigma(Z) \cdot B$ (pb)	$226 \pm 22 \pm 18 \pm 15$	$209 \pm 13 \pm 9 \pm 14$	$214 \pm 11 \pm 14 \pm 15$
R	$9.8 \pm 1.1 \pm 0.4$	$10.2 \pm 0.8 \pm 0.4$	$10.0 \pm 0.6 \pm 0.4$
$B.R.^{-1}(W)$	9.9 ± 1.2	9.5 ± 0.9	9.6 ± 0.7
M_{top}, 90% C.L.	-	> 48 GeV/c^2	> 49 GeV/c^2
M_{top}, 95% C.L.	> 22 GeV/c^2	> 43 GeV/c^2	> 45 GeV/c^2
$\Gamma(W)/\Gamma(Z)$	0.89 ± 0.11	0.86 ± 0.08	0.87 ± 0.07
g_μ/g_e			1.01 ± 0.04

Table 5: CDF results on $\sigma \cdot B$ for $W \to \mu\nu$ and $Z \to \mu\mu$.

the number of Z's collected. The goal for this run is to log enough data to bring the statistical error down to the level of the systematic error. Two measurements to look for are:

- $W^{\pm}$ *Mass Measurement:* CDF and DØ want to achieve an error on M_W of order ± 100 MeV with 100 pb^{-1}. Figure 21 shows the relationship between M_W and the top mass for several Higgs masses. If 1000 GeV is taken as an upper limit for M_H, then a precision W mass measurement puts an upper bound on M_t. More optimistically, if M_W is measured to ± 100 MeV and M_t determined to ± 5 GeV, then it is possible to get a (limited) handle on the Higgs mass.

- *Lepton Asymmetry in W Decays:* is sensitive to parton distribution functions at the low x and high Q^2 scale of W production. The asymmetry for the leptons from $W \to \ell\nu$ as a function of rapidity is defined as

$$A(y) = \frac{d\sigma(\ell^+)/dy - d\sigma(\ell^-)/dy}{d\sigma(\ell^+)/dy + d\sigma(\ell^-)/dy} \ .$$

Results from CDF [27] are shown in Fig. 22 where it is clear that additional statistics will be essential to discriminate among parton distribution functions. With their good rapidity coverage for muons, DØ will also contribute to this measurement.

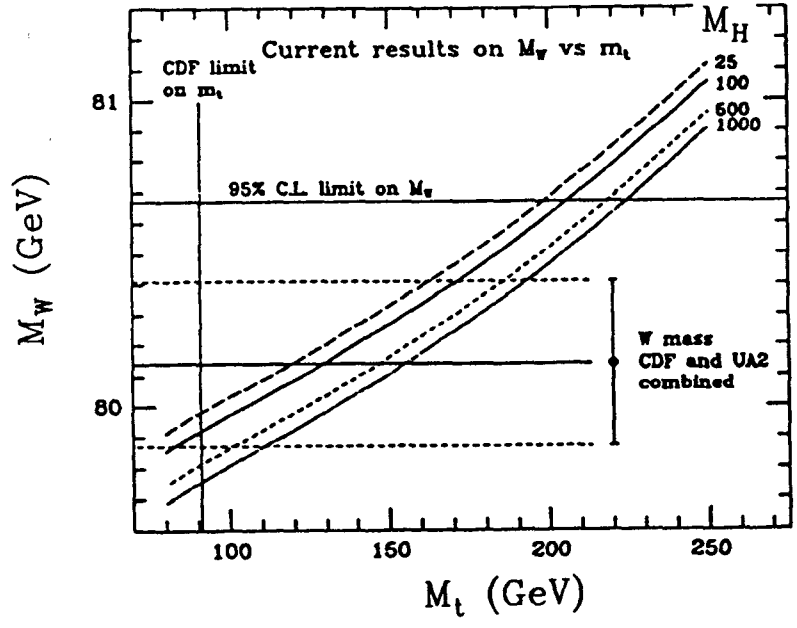

Figure 21: Standard Model prediction for the relation of the W, top and Higgs masses. Also shown are the current combined CDF and UA2 M_W measurements and limit on M_t.

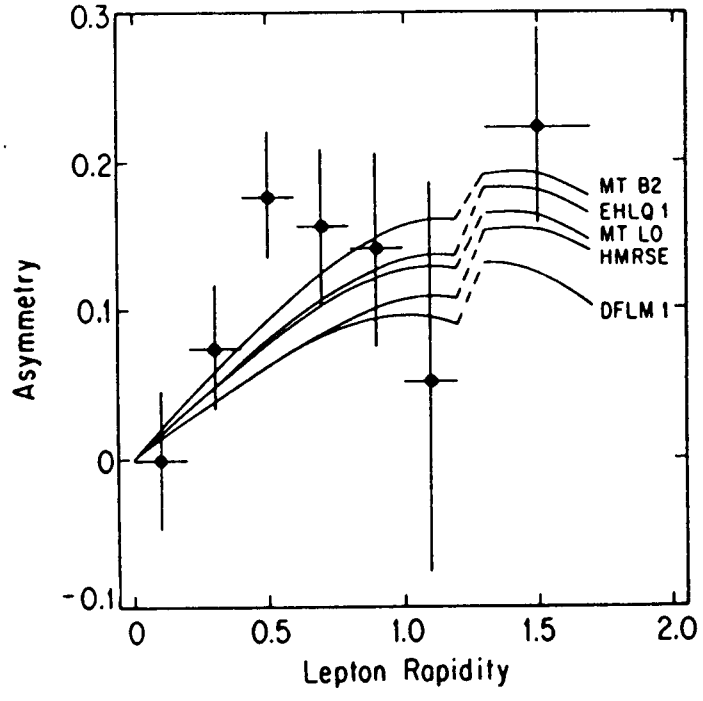

Figure 22: The lepton asymmetry $A(y)$ for $W \rightarrow \ell\nu$ events. The curves are the predictions for a representative set of parton distribution functions. They are discontinuous due to different cuts for central and forward leptons.

6 Summary and Outlook

DØ and CDF are on the air and will take data until the end of 1993. This run is expected to result in a factor of 20 increase in integrated luminosity over that previously logged by CDF. The combination of two detectors and a large data set will greatly extend the physics reach at $\sqrt{s} = 1.8$ TeV. The rich physics menu available with $\int \mathcal{L}\, dt = 100\ pb^{-1}$ is headed by the search for the top quark where the experiments hope to be sensitive to top masses up to ≈ 150 GeV. The promising early results from CDF have shown that bottom physics is a new, productive avenue of research in hadron colliders. The emergence of higher order QCD calculations and precise jet data allows experiment to confront theory in an increasingly quantitative way. The determination of the $W^{\pm}$ mass to 100 MeV leads the list of electroweak measurements which will further our understanding of the Standard Model. With the highest center-of-mass energy in the world, searches for unknown/unexpected exotic particles will continue to exclude the phase space available to new theories or (hopefully!) find something new. With these prospects, the next few years will be exciting and fruitful for collider physics at Fermilab.

References

[1] F. Abe *et al.*, Nucl. Instr. and Meth. A271 (1988) 387.

[2] F. Abe *et al.*, Phys. Rev. D **45** (1992) 3921.

[3] B. Barnett *et al.*, Nucl. Instr. and Meth. A315 (1992) 125.

[4] Design Report, the DØ Experiment at the Fermilab Antiproton–Proton Collider (1984).

[5] S. Abachi *et al.*, FERMILAB-PUB-92/162, 1992, submitted to Nucl. Instr. and Meth. A.

[6] C. Brown *et al.*, Nucl. Instr. and Meth. A279 (1989) 331.

[7] J.M. Butler *et al.*, Nucl. Instr. and Meth. A290 (1990) 122.

[8] D. Green *et al.*, Nucl. Instr. and Meth. A244 (1986) 356.

[9] R. Hollebeek, "Experimental Studies of Top Quarks," these proceedings.

[10] See, for example, J. Ellis, G.L. Fogli, and E. Lisi, CERN-TH. 6568/92, 1992.

[11] R.K. Ellis, FERMILAB-Pub-91/30-T, 1991.

[12] F. Abe *et al.*, Phys. Rev. Lett. **68** (1992) 3398.

[13] R. Wagner *et al.*, in "Physics at Fermilab in the 1990's," Breckenridge, Colorado, August 15-24, (1989) 181 (Eds. D. Green and H. Lubatti.)

[14] E.W.N. Glover, A.D. Martin, and W.J. Stirling, Z. Phys. C38 (1988) 473.

[15] F. Abe *et al.*, Phys. Rev. Lett. **68** (1992) 3403.

[16] Particle Data Group, Phys. Rev. D **45** (1992).

[17] C. Albajar *et al.*, Phys. Lett. B **273** (1991) 540.

[18] A. Gauthier (CDF Collaboration), FERMILAB-Conf-92/112-E, 1992.

[19] R. Ellis and J. Sexton, Nucl. Phys. **B269** (1986) 445; F. Aversa *et al.*, Phys. Lett. **B 210** (1988) 225; S. Ellis, Z. Kunszt, and D. Soper, Phys. Rev. Lett. **62** (1989) 2188; S. Ellis, Z. Kunszt, and D. Soper, Phys. Rev. Lett. **64** (1989) 2121.

[20] F. Abe *et al.*, Phys. Rev. Lett. **68** (1992) 1104.

[21] J. Alitti *et al.*, Phys. Lett. **B 257** (1991) 232.

[22] F. Abe *et al.*, Phys. Rev. Lett. **68** (1992) 2734.

[23] P. Aurenche *et al.*, in "Physics at Fermilab in the 1990's," Breckenridge, Colorado, August 15-24, (1989) 212 (Eds. D. Green and H. Lubatti.)

[24] B. Flaugher (CDF), FERMILAB-Conf-92/24-E, to be published in "XXI International Symposium on Multiparticle Dynamics," Wuhan, China, September 23-27, 1991.

[25] F. Abe *et al.*, Phys. Rev. **D 44** (1991) 29.

[26] F. Abe *et al.*, Phys. Rev. Lett. **69** (1992) 28.

[27] F. Abe *et al.*, Phys. Rev. Lett. **68** (1992) 1458.